IET Electrical Systems in Transportation

Research Article

IET Journals
The Institution of Engineering and Technology

Single-stage ZETA-SEPIC-based multifunctional integrated converter for plug-in electric vehicles

ISSN 2042-9738
Received on 26th June 2017
Revised 21st September 2017
Accepted on 10th October 2017
E-First on 30th October 2017
doi: 10.1049/iet-est.2017.0063
www.ietdl.org

Ankit Kumar Singh[1] ✉, *Mukesh Kumar Pathak*[1]

[1]*Department of Electrical Engineering, IIT Roorkee, Roorkee 247667, India*

✉ *E-mail: ankitee04@gmail.com*

Abstract: A single-stage-based integrated power electronic converter has been proposed for plug-in electric vehicles (PEVs). The proposed converter achieves all modes of vehicle operation, i.e. plug-in charging, propulsion and regenerative braking modes with wide voltage conversion ratio (M) [$M < 1$ as well as $M > 1$] in each mode. Therefore, a wide variation of battery voltage can be charged from the universal input voltage (90–260 V) and allowing more flexible control for capturing regenerative braking energy and dc-link voltage. The proposed converter has least components compared to those existing converters which have stepping up and stepping down capability in all modes. Moreover, a single switch operates in pulse width modulation in each mode of converter operation hence control system design becomes simpler and easy to implement. To correctly select the power stage switches, a loss analysis of the proposed converter has been investigated in ac/dc and dc/dc stages. Both simulation and experimental results are presented to validate the operation of the converter.

1 Introduction

The electric vehicles or plug-in electric vehicles (PEVs) are now a promising solution to curb the air pollution that uses pollution-free battery power to produce clean energy for the vehicle [1]. The PEVs are combination of on-board charger, battery, and the inverter-drive system [2–5]. In majority of PEVs, a bidirectional dc/dc converter is interfaced between the battery and dc-link of machine inverter [6–8] for power flow during propulsion and regenerative braking operation. Therefore, an individual ac/dc converter is used to charge the battery from the grid side. In this conventional structure, two separate power electronic converters are needed for two independent operations (charging and discharging of the battery). The bidirectional dc/dc converter in conventional structure can be integrated with the on-board charger, to have one power electronics interface for complete operation of PEVs. The overall block diagram of an integrated charger with single power electronic is shown in Fig. 1*a*. This integration reduces the number of components because some of the switches and inductors are utilised both in ac/dc and dc/dc stages. Therefore, reduced number of switches and inductors lead to higher power density, compact size and lower cost. In this regard, this paper proposes, a new ZETA-SEPIC-based integrated converter for PEVs, as shown in Fig. 1*b* which has buck/boost capability in each mode of operation. In addition, buck/boost operation in each mode allows selection of wide range of the battery voltage, efficient control of dc-link voltage and capturing the regenerative braking with a wide variation of the motor speed.

A comparison of existing integrated converters and other competitive converters with respect to the proposed converter is described in the following paragraph.

An integrated converter in [9] utilises a number of semiconductor devices to achieve each mode; therefore, it may not be an efficiency optimised and cost-effective solution. In addition, the presence of a large number of devices, this converter requires a complex control strategy to turn on the switches. An integrated converter in [10] has only boost charging capability; thus, the selection of wide range of battery voltages is compromised. In [11], an integrated converter does not have buck/boost operation in any mode; thus, selection of the dc-link and battery voltage range is sacrificed. A three-level quasi two-stage converter in [12] with two inductors has buck/boost operation only in charging mode as a result, aforementioned advantages of buck/boost operation in each mode is sacrificed. In [13, 14], an SEPIC-based converter has been proposed for the battery charging using three inductors and at least one extra inductor is also required for propulsion and regenerative braking modes. Thus, the increase of magnetic components has a negative effect on weight, cost and volume of the charger. Authors in [15, 16] have proposed a CuK converter based on-board battery charger, which operates only in charging mode, does not include propulsion and regenerative braking modes. A single-stage converter in [17] operates only battery charging mode using four switches, eight diodes and two inductors. However, to achieve other modes of the vehicle, some more components will be employed. Therefore, this converter will utilise a large number of active and passive components, which will have an adverse effect

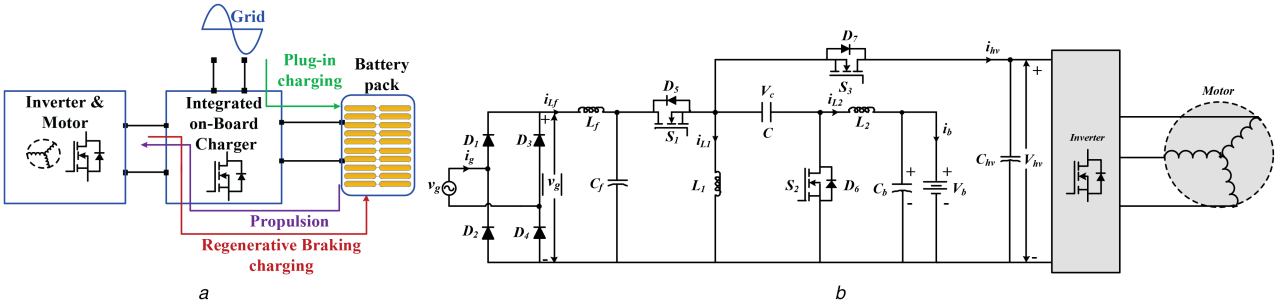

Fig. 1 *Block diagram and proposed structure of the integrated converter*

(a) Block diagram of PEV with on-board integrated battery charger, ***(b)*** Proposed ZETA-SEPIC-based integrated converter for PEVs

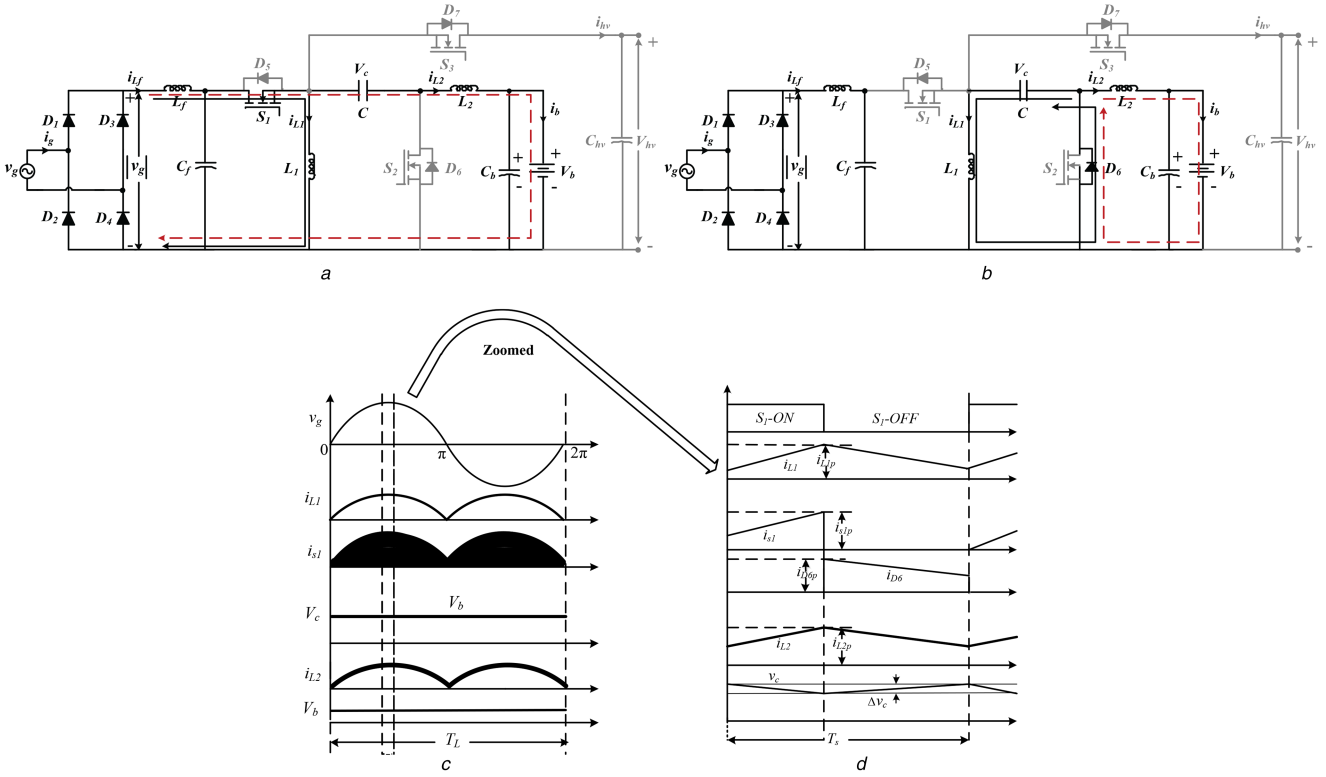

Fig. 2 *Equivalent operating circuits and theoretical waveforms of plug-in charging mode*
(a) Battery charging from the grid, when switch S_1 is turned ON and, ***(b)*** when switch S_1 is turned OFF, ***(c)*** Waveforms during one-line cycle, ***(d)*** One switching cycle

on cost and compactness of the charger. Authors in [18] have proposed front-end power factor correction (PFC) converter for EV battery charger, which is a bridgeless type converter that uses four inductors and at least one additional inductor requires to achieve other modes of the vehicle. A single-stage-based inductive charger has been proposed in [19] that provides a wide range voltage for battery charging, but this converter uses a large number of passive components and semiconductor devices; therefore, the floor area of the charger will increase and less suitable for on-board application of PEVs.

Motivation of the work: The universal voltage range of single phase is around 90–260 V and a majority of commercially available battery voltage range are between 200 and 450 V [20–22]. Therefore, the buck/boost operation of converter is needed in plug-in charging mode for universal voltage supply. Moreover, in propulsion mode, usually, the battery voltage is stepped up to the dc-link voltage (inverter dc-link voltage) to propel the motor drive system. In a case of high state of charge (SOC) of the battery, the battery voltage may be more than the dc-link voltage, in such case, the dc/dc converter with buck operation is required. Furthermore, in regenerative braking, a step-down operation is typically required because the dc-link voltage usually higher or near to the battery voltage. However, at low speed, boost operation is also required to capture all the available regenerative braking energy. It is explained as: at a lower speed, the propulsion machine induces lower back electromotive force. If the generated voltage across the motor terminals is lower than the battery voltage, a bidirectional converter between the propulsion inverter and the battery must have boosting capability [10]. Therefore, the buck/boost capability of converter is also needed during regenerative braking operation. Hence, it is concluded that buck/boost operation of converter is essential in each mode of vehicle operation.

2 Operation of the proposed converter

The proposed integrated converter operates in three modes: battery charging from the grid (plug-in charging), propulsion, and regenerative braking of charging. In the following section, operation of converter is discussed in detailed manner.

2.1 Plug-in charging mode

The plug-in charging mode of vehicle is possible only when vehicle is not in motion and then charger plug is connected to single phase supply socket to charge the battery.

In this mode, the proposed converter operates as ZETA PFC converter and switch S_1 is pulse width modulation (PWM) gated while switch S_2 and S_3 are in OFF-state. When switch S_1 is turned ON, inductor L_1 stores energy through the path $|v_g|$-L_f-S_1-L_1-$|v_g|$ and inductor L_2 stores energy through the path $|v_g|$-L_f-S_1-C-L_2-V_b-$|v_g|$, as shown in Fig. 2*a*. When switch S_1 is turned OFF, inductor L_1 discharges by supplying its stored energy to the capacitor C, and voltage across capacitor gradually increases, which is shown in Fig. 2*d*, and this capacitor is charged to the battery voltage V_b. While inductor L_2 supplies energy to the output stage (capacitor and battery) shown in Fig. 2*b* and current through L_2 decreases linearly, as shown in Fig. 2*d*. The capacitor C_{hv} is charged to $V_{g,max}$ through the body diode of S_3 in very short duration then after it retains this value forever in this mode. If the duty ratio of the converter is d_1 then voltage-second balance either of inductor L_1 or L_2 for one switching period, T_s, can be given as

$$V_{gmax}|\sin(\omega t)| * d_1(t) = V_b * (1 - d_1(t)) * T_s \quad (1)$$

From (1), the voltage conversion ratio M_1 as

$$M_1 = \frac{V_b}{V_{gmax}|\sin \omega t|} = \frac{d_1(t)}{1 - d_1(t)} \quad (2)$$

2.2 Propulsion mode

When this mode begins, battery started supplying power to the dc-link of the inverter and vehicle comes in running mode. During motion of the vehicle, the SOC of the battery continuously decreases. In this mode, switches S_1 and S_3 are kept in OFF state using mode selector logic, and switch S_2 is gated through PWM signal. When switch S_2 is turned ON, inductor L_2 stores energy through the path V_b-L_2-S_2-V_b, and capacitor C discharges through inductor L_1, as shown in Fig. 3*a* and inductor current through L_1 is

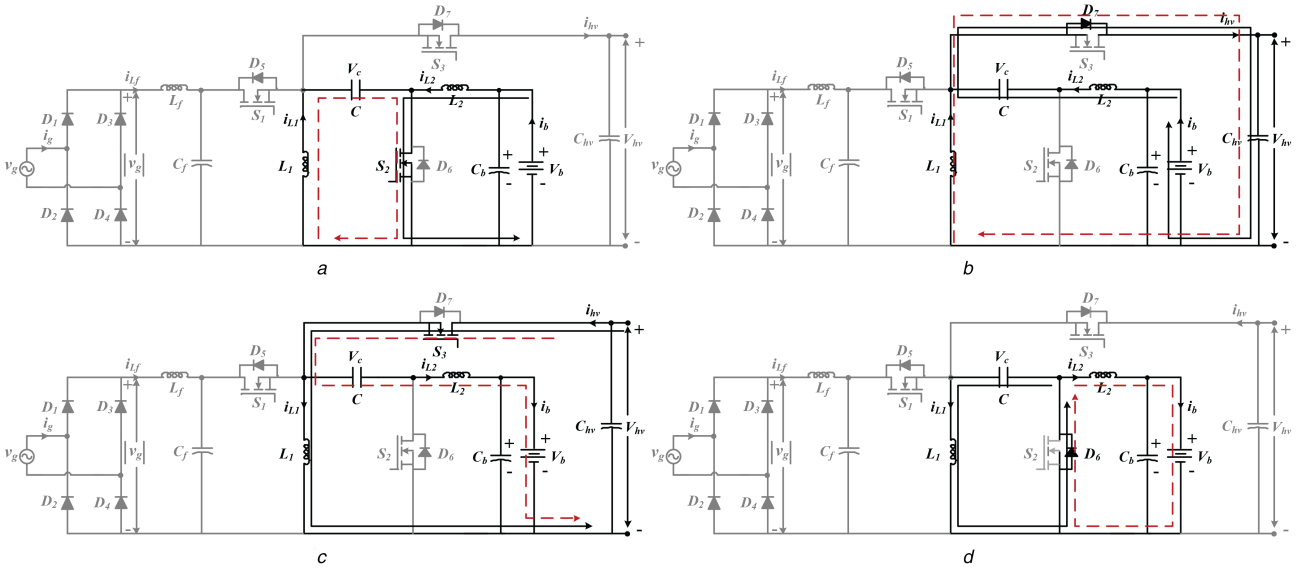

Fig. 3 *Equivalent operating circuits during propulsion and regenerative braking modes*
(a) Propulsion mode of operation, when switch S_2 is ON, ***(b)*** When switch S_2 is OFF, ***(c)*** Operation of regenerative braking, when switch S_3 is ON, ***(d)*** When switch S_3 is OFF

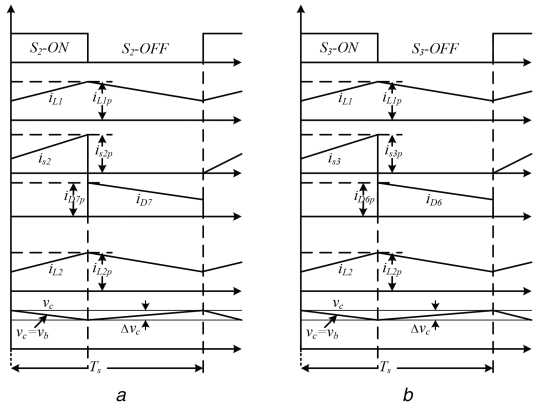

Fig. 4 *Switching waveforms*
(a) In propulsion mode, ***(b)*** In regenerative braking mode

linearly increasing, which is shown in Fig. 4*a*. When S_2 is turned OFF, inductor L_2 transfers its stored energy in the capacitor C and dc-link capacitor C_{hv} through the path V_b-L_2-C-D_7-V_{hv}-V_b and capacitor C is charged to the battery voltage. The inductor L_1 transfers its stored energy to the dc-link through the path L_1-D_7-V_{hv}-L_1, as shown in Fig. 3*b*, and current through L_1 gradually decreases, which is shown in Fig. 4*a*. If the duty ratio of the converter is d_2 and applying voltage-second balance either in inductor L_1 or L_2 for one switching period then one can obtain:

$$V_b * d_2 * T_s = V_{hv} * (1 - d_2) * T_s \tag{3}$$

The voltage conversion ratio M_2 from (3) can be expressed as

$$M_2 = \frac{V_{hv}}{V_b} = \frac{d_2}{1 - d_2} \tag{4}$$

2.3 Regenerative braking mode

Operation of regenerative braking mode is similar to the grid mode operation, when switch S_3 is turned ON, inductor L_1 stores energy through the path V_{hv} S_3-L_1-V_{hv} and inductor L_2 stores energy through the path V_{hv}-S_3-C-L_2-V_b-V_{hv}, as shown Fig. 3*c*. When S_3 is turned OFF L_1 transfers its stored energy to the capacitor (C) through the path C-L_1-D_6 as shown in Fig. 3*d* and capacitor voltage V_c gradually increases, which is shown in Fig. 4*d*. While, L_2 transfers its stored energy to capacitor C_b and battery (Fig. 3*d*). If the duty ratio of the converter is d_3 by applying voltage-second balance either of inductor L_1 or L_2, and one can obtain:

$$V_{hv} * d_3 * T_s = V_b * (1 - d_3) * T_s \tag{5}$$

The voltage conversion ratio M_3 from (5) can be expressed as

$$M_3 = \frac{V_b}{V_{hv}} = \frac{d_3}{1 - d_3} \tag{6}$$

3 Component selection

3.1 Selection of semiconductor devices

Usually, power rating of each mode of PEVs is not same due to that the selection of switch ratings, i.e. voltage/current are decided by particular mode of operation. Therefore, voltage/current ratings of a particular switch will be selected as peak voltage/current developed either in switch or its body diode conduction. Table 1 shows peak voltage and current stresses of switch in all modes. From Table 1, switch ratings are selected as follows:

Peak voltage rating of S_1 and $S_2 = \max(|v_{gmax}| + V_b, (V_b + V_{hv})$, and peak current rating $S_1 = i_{gmax}| + I_b$. The peak current rating of $S_2 = \max(|i_{gmax}| + I_b, I_b + I_{hv})$. While voltage and current ratings of S_3 are chosen same as S_2 because body diode of S_3 conducts in propulsion mode and power rating of propulsion mode in PEVs usually highest among all modes.

3.2 Selection of inductors L_1 and L_2

In the PEVs, the power level is usually high. At high-power-level continuous conduction mode (CCM) is preferred compared to discontinuous mode (DCM) since current stress in CCM are much smaller than DCM. During time interval $[0, d_1(t)T_s]$, the inductor current ripple of L_1 can be written as

$$\Delta i_{L1} = \frac{|v_g|}{L_1} d_1(t) T_s \tag{7}$$

Boundary condition for inductor current ripple happens when current ripple is the twice of the average input current. Thus,

$$\Delta i_{L1} = \frac{|v_g|}{L_1} d_1(t) T_s = 2 i_g \tag{8}$$

Table 1 Voltage and current ratings of switches in all modes

Modes	S_1		S_2		S_3	
	Voltage	Current	Voltage	Current	Voltage	Current
plug-in charging	$\lvert v_{g,\max}\rvert + V_b$	$\lvert i_{g,\max}\rvert + I_b$	$\lvert v_{g,\max}\rvert + V_b$	$\lvert i_{g,\max}\rvert + I_b$	$\lvert v_{g,\max}\rvert + v_c$	NC
propulsion	$V_{hv} + V_b$	NC	$V_{hv} + V_b$	$I_b + I_{hv}$	$V_{hv} + V_b$	$I_b + I_{hv}$
regenerative braking	$V_{hv} + V_b$	NC	$V_{hv} + V_b$	$I_b + I_{hv}$	$V_{hv} + V_b$	$I_b + I_{hv}$

NC, not conducting.

Table 2 Simulation circuit parameters

Simulation specifications: SET1/SET2	
grid voltage (V_g)	220/70.7 V
DC-link voltage (V_{hv})	400/100 V
line frequency (f_L)	50/50 Hz
battery nominal voltage (V_b)	300/60 V
nominal charging power (P_b)	1 kW/230 W
L_1/L_2	2/2 mH
switching frequency (f_s)	20/20 kHz
$C_{hv}/C/C_b$	SET1 = SET2 = 550/10/2200 μF

Assuming unity power factor, the ratio of input voltage and input current can be expressed by an effective resistor, R_e

$$R_e = \frac{v_g}{i_g} = \frac{V_g^2}{p_g} \tag{9}$$

Thus, (CCM) condition for inductor current (i_{L_1}) can expressed as

$$L_1 > \max\left(\frac{R_e d_1(t)}{2f_s}\right) > \frac{V_g^2}{p_g}\frac{1}{2f_s}\frac{V_b}{|V_{g,\max}| + V_b} \tag{10}$$

From (10), larger the minimum input power $P_{g,\min}$ and switching frequency f_s is, the easier the converter can enter in CCM. Similarly, the boundary condition for L_2 can be derived. The CCM condition for inductor current i_{L_2} can be calculated as

$$L_2 > \left(\frac{R_L d_1'(t) T_s}{2}\right) > \frac{R_{L,\max}}{2}\frac{|V_{g,\max}|}{|V_{g,\max}| + V_b}\frac{1}{2f_s} \tag{11}$$

According (11), higher the switching frequency and smaller load resistance, $R_{L,\max}$ is, the easier the converter can enter in CCM mode. Using specification given in Table 2, inductors L_1 and L_2 are selected as 2 mH in the simulation as well as in hardware.

3.3 Selection of capacitor C

The coupling capacitor C is an important element in the proposed converter since its value greatly influence the quality of input current. Therefore, this capacitor will be designed under the following constraints: The resonant frequency of L_1, L_2 and C during CCM operation must be greater than line frequency f_L to avoid input current oscillations at every half line cycle and lower than switching frequency f_s to assure constant voltage in a switching period, i.e.

$$f_L < f_r < f_s \tag{12}$$

where

$$f_r = \frac{1}{2\pi\sqrt{(L_1 + L_2)C}} \tag{13}$$

In this work, switching frequency (f_s) is set as 20 kHz, and f_r is set as 1 kHz. The capacitor C is selected as 10 μF both in simulation and hardware. The voltage rating of this capacitor is selected based on battery voltage range because both in ZETA mode or SEPIC modes, the voltage across coupling capacitor follows battery voltage with ripple.

3.4 Selection of L_f and C_f

The design of input filter is essential for maintaining low harmonic distortion in grid current [23, 24]. The maximum value of filter capacitance is expressed as

$$C_{f_{\max}} = \frac{I_{g,\max}\tan\theta}{2\pi f_L V_{g,\max}} \tag{14}$$

where $V_{g,\max}$ and $I_{g,\max}$ are peak input voltage, and θ is considered below 5° for maintaining high input power factor. The capacitance $C_{f_{\max}}$ is calculated as 1.14 μF and selected value in the simulation and hardware is 1 μF.

The filter inductor to maintain low ripple is calculated as

$$L_f = \frac{1}{4\pi^2 f_c^2 C_f} \tag{15}$$

where f_c is cut off frequency, which is selected such that it should more than the grid frequency $f_L = 50$ Hz and less than switching frequency $f_s = 20$ kHz. Therefore, it is chosen as 4 kHz. L_f from (15) is calculated as 1.58 mH, and the selected value in the simulation and hardware is 1.5 mH.

3.5 Selection of capacitor C_b

With regards to the parallel capacitor across the battery terminal, the switching frequency voltage ripple is negligible as this capacitor is typically very large. Twice of the line frequency voltage ripple is more critical since it directly affects the charging voltage. The low-frequency voltage ripple on the battery capacitor is given [25] as

$$C_{b,\min} > \frac{P_b}{4f_L \Delta v_b V_b} \tag{16}$$

where f_L is the grid frequency and Δv_b is the capacitor ripple. To reduce the low-frequency voltage ripple, a large value of capacitor is preferred. However, this will make the electrolytic capacitor bulky. Therefore, the trade off between output voltage ripple and capacitor size must be taken into consideration for designing the converter. From above expression, the dc-link capacitance is selected as 2.2 mF for $\Delta v_b < 5\%$ of the battery voltage.

4 Loss analysis

Due to high-power application of the proposed converter, it is necessary to estimate the semiconductor power losses of the converter in each mode to correctly select the power stage components. The conduction and switching losses for two semiconductor devices, i.e. 1200 V/100 A and 1700 V/72 A in ac/dc (plug-in charging) and dc/dc (propulsion) stages are analytically calculated using manufacturers date sheets. Moreover, the passive components that come in main current path are also presented in this analysis to accurately find efficiency of the converter in operation modes. The conduction loss for an MOSFET switch can be calculated as follows:

Table 3 Semiconductors and passive components losses of the proposed converter in ac/dc and dc stages with $V_b = 300$ V and $V_{hv} = 400$ V

P_{ch}, kW	$P_{dc/dc}$, kW	V_{grid}, V	Switch rating	Total semiconductors losses (P_S), W		Total passive components losses (P_P), W	
				ac/dc stage	dc/dc stage	ac/dc stage	dc/dc stage
1.8	5	120	1200 V/100 A [V_F = 2.55 V, t_r = 65, t_f = 80]	59	100.94	44.88	47.254
3.2	5	240		68.93	100.94	48.69	47.254
1.8	10	120	1200 V/100 A [V_F = 2.55 V, t_r = 65, t_f = 80]	59	207.39	40.13	189.079
6.6	10	240		154.11	207.39	185.445	189.079
1.8	5	120	1700 V/72 A [V_F = 3.6 V, t_r = 20, t_f = 18]	33.44	78.95	44.88	47.254
3.2	5	240		46.18	78.95	48.69	47.254
1.8	10	120	1700 V/72 A [V_F = 3.6 V, t_r = 20, t_f = 18]	33.44	201.66	44.88	189.079
6.6	10	240		126.45	201.66	185.445	189.079

Table 4 Loss breakdown of the system in ac/dc (plug-in charging) and dc/dc (propulsion) stages with 400 V dc-link and 300 V battery

Stage		$P_{S,cond}$, W	P_{sw}, W	P_D, W	P_{L_f}, W	P_{L_1}, W	P_{L_2}, W	P_c, W
ac/dc stage	[120 V,1.8 kW]	33.55	18	7.45	13.5	24.75	5.63	1
	[240 V, 6.6 kW]	65	56.62	31.32	45.375	73.18	65.81	1.08
dc/dc stage	[5 kW]	39.75	29.49	31.7	—	17.18	28.98	1.094
	[10 kW]	79.4	58.99	69	—	68.75	115.95	4.379

$$P_{S,cond} = I_{s,rms}^2 * R_{(on)} \tag{17}$$

On other hand, the conduction loss for an IGBT switch will be calculated as

$$P_{S,cond} = \langle i_s \rangle_{T_s} * V_{CE_{sat}} \tag{18}$$

Switching energy losses occur due to the simultaneous presence of significant drain-source voltage and drain current during each transient from turn-off state to turn-on state, and from turn-on state to turn-off state. Then total switching power losses of a switch can be approximately calculated as

$$P_{sw} = \frac{1}{2}(V_{s,max} * I_{s,max}) * (t_r + t_f) * f_s \tag{19}$$

where $V_{s,max}$ and $I_{s,max}$ are peak values of voltage and current and t_r and t_f are the rising and falling times of a switch, respectively. Power loss of diode is the sum of diode conduction loss (product of average current (I_F) and knee voltage (V_F)) and reverse recovery loss, which is modelled as

$$P_D = V_F * I_F + P_{Qrr} \tag{20}$$

where P_{Qrr} is the reverse recovery loss of a diode. The P_{Qrr} can be neglected for fast recovery diode and lower switching frequency. The total semiconductor losses are modelled as

$$P_S = P_{S,cond} + P_{sw} + P_D \tag{21}$$

The passive components that come in main current path are L_1, L_2, L_f and capacitor C, then inductors copper losses are modelled as

$$P_L = I_{L_f,rms}^2 * r_f + I_{L_1,rms}^2 * r_1 + I_{L_2,rms}^2 * r_2 \tag{22}$$

where r_f, r_1 and r_2 are series resistances of inductors L_f, L_1 and L_2, respectively.

The ohmic loss in equivalent series resistance r_c of the capacitor C is expressed as

$$P_c = I_{c,rms}^2 * r_c \tag{23}$$

Then total passive component losses P_P is written as

$$P_P = P_{L_f} + P_{L_1} + P_{L_2} + P_c \tag{24}$$

where P_{L_f}, P_{L_1} and P_{L_2} are the copper loss in L_f, L_1 and L_2, respectively.

With the help of these loss equations, Table 3 shows total losses of semiconductor devices (P_S) and passive components (P_P) in charging (ac/dc stage) and propulsion (dc/dc stage) modes, where P_{ch} and $P_{dc/dc}$ denote power rating of charging and propulsion modes, respectively. It is noticed that from Table 3 in plug-in charging mode (ac/dc), semiconductor losses with grid voltage of 240 V are around 1.5–2.2% of the rated powers for mentioned switching devices. While with 120 V grid supply, total losses in charging are found between 2 and 4% of the rated power. However, the total losses in dc/dc stage are around 2.5–3.1% of the rated powers ($P_{dc/dc} \leqslant 10$ kW).

The passive components losses P_P in ac/dc stage with 120 V grid supply is 2.5% of the rated power while with 240 V grid voltage is 1.5–2.78% of the rated powers. In dc/dc stage, P_P is around 1–2% of the rated powers. The percentage of passive component losses in dc/dc stage is slightly lower than the ac/dc stage, it is due to fact that inductor L_f copper loss is not present in dc/dc stage. Moreover, the total losses (semiconductors and passive components) in ac/dc and dc/dc stages are between 5–5% and 2–4% of the rated powers with both devices, respectively. A loss breakdown of the converter system at full load for 1200 V/100 A switch is given in Table 4.

5 Comparative analysis of the proposed converter with single-stage converters

The conventional single-stage battery charger topologies, namely the boost PFC converter, inverting buck/boost PFC converter, SEPIC PFC converter, and CuK PFC converter is shown in Fig. 5. In order to have a fair comparison of the proposed converter with these single-stage converters, the dc/dc converter connected between the battery and dc-link in Fig. 5, is assumed to be a four-quadrant bidirectional converter. The boost PFC converter can only charge the battery when battery voltage is more than the peak grid voltage ($V_b > V_{g,max}$). While inverting buck/boost and CuK converter both have negative output voltage with respect to the input. The same polarity between the input and the output has an advantage of solving electromagnetic interference/electromagnetic compatibility problems, and in designing filters easily, because the internal ground of a vehicle, the ground of the on-board battery charger (OBC) and the cathode of the battery can have the same

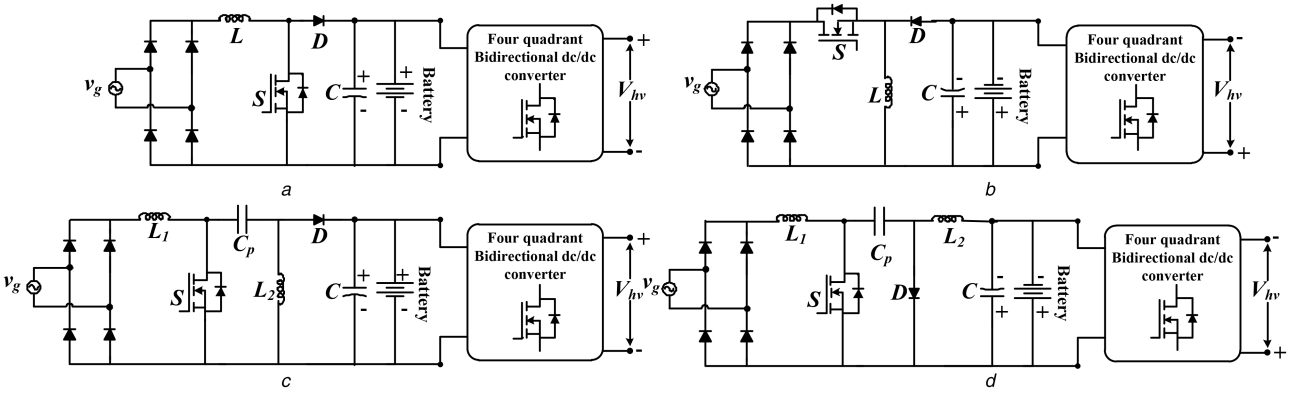

Fig. 5 *Conventional single-stage EV battery chargers*
(a) Boost PFC converter, ***(b)*** Inverting buck/boost PFC converter, ***(c)*** SEPIC PFC converter, ***(d)*** CuK PFC converter

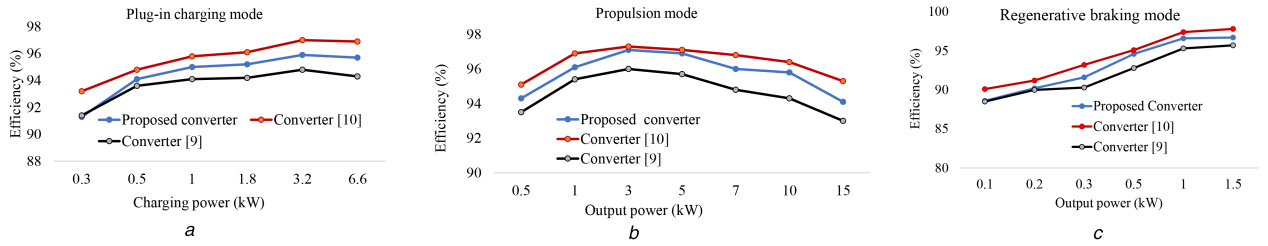

Fig. 6 *Efficiency comparison of the proposed converter in*
(a) Plug-in charging mode, ***(b)*** Propulsion mode, ***(c)*** Regenerative braking mode

Table 5 Comparative study of the proposed charger with single-stage chargers

Converter topologies	Modes of operation			Switch	Diode	Inductor	Capacitor
	Plug-in charging	Propulsion	Regenerative braking				
boost PFC converter	boost	buck/boost	buck/boost	5	5	2	2
inverting buck/boost PFC converter	buck/boost	buck/boost	buck/boost	5	5	2	2
SEPIC PFC converter	buck/boost	buck/boost	buck/boost	5	5	3	3
CuK PFC converter	buck/boost	buck/boost	buck/boost	5	5	3	3
integrated converter [9]	buck/boost	buck/boost	buck/boost	6	9	1	2
integrated converter [10]	boost	buck/boost	buck/boost	4	4	1	2
integrated converter [11]	boost or buck/boost (negative half cycle)	boost	buck	5	1	1	2
proposed integrated converter	buck/boost	buck/boost	buck/boost	3	4	2	3

potential [17]. However, in CuK and SEPIC PFC-based converter topologies have one additional inductor compared to the proposed integrated converter. In addition to these conventional chargers, other existing integrated chargers are also included in comparative analysis. It can be noticed from Table 5, the proposed converter has least components compared to those converters which have buck/boost operation in each mode. However, the integrated converter [9] has lower voltage and current stresses across the devices (either input or output voltage and current) in each mode as well as buck/boost operation in each mode, but the efficiency of this converter sacrifices because three to four semiconductor devices come in the main current path. The integrated converter [10] has low stresses (voltage and current) like converter [9], but the major limitation of this converter is only to have a boost charging capability hence selection of the wide range of battery voltage is not possible. The efficiency plots of the proposed converter and integrated converters of [9, 10] using 1200 V/100 A device and 220 V grid voltage in each mode are shown in Fig. 6. The integrated converter [11] has bridge less nature in plug-in charging mode as well as low-voltage and current stresses in propulsion and regenerative modes and one–two devices come in current path; therefore, this converter will have higher efficiency than proposed converter in each mode. However, the major limitation of this converter is none of the modes have buck/boost operation.

From Table 5, the proposed converter has two additional passive components (one inductor and one intermediate capacitor C) compared to other existing integrated converters. The voltage across capacitor C follows battery voltage both in SEPIC and ZETA modes, the peak voltage across the capacitor $C = V_b + \Delta V_C$, where ΔV_C is voltage ripple of V_C then voltage rating of this capacitor is selected according to slightly higher than the battery voltage. Usually, the capacitance value of C is between 0.5 and 10 μF for 20 kHz switching frequency range [23, 26]; therefore, the size of this capacitor is smaller compared to battery terminal capacitor C_b (designed based on twice of the grid frequency). Nevertheless, the additional increase of two passive components as well as higher losses in the proposed converter compared to existing converters [10, 11] results increase in a volume of the proposed converter. However, converter [9] has a number of semiconductor devices (switches are twice of the proposed converter) and switches with driver circuit occupy a considerable floor area as well as higher losses, result in the overall size of the proposed converter may be lower or comparable to this converter. Moreover, compared to conventional single-stage converters which have buck/boost operation in each mode, the proposed converter has lower volume due to lower passive and semiconductor components.

6 Control system design

The control structure during different modes of converter operation [10] is shown in Fig. 7. Each mode is implemented by mode selector logic, which requires external input such as torque (τ),

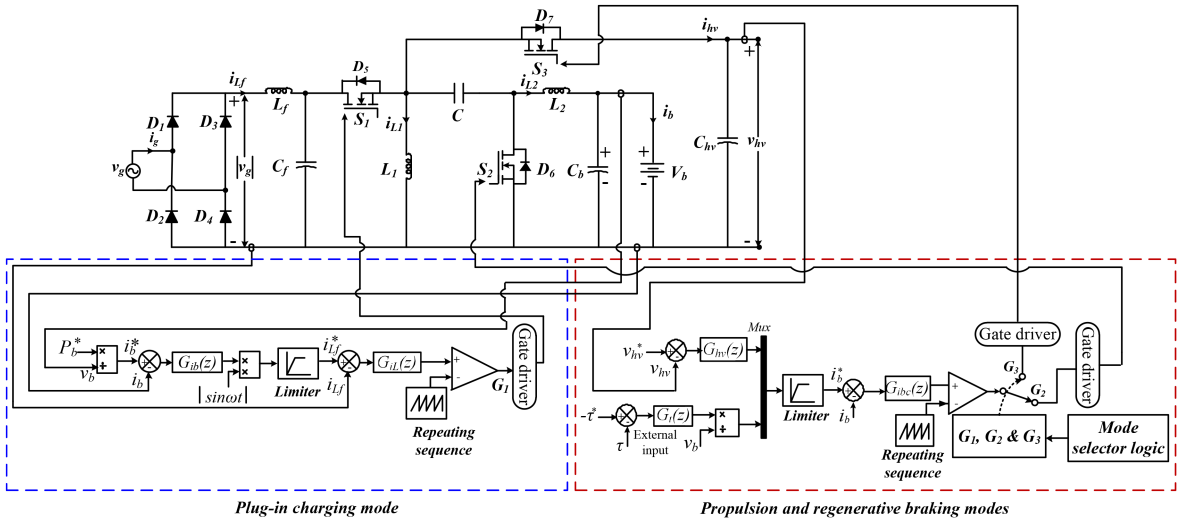

Fig. 7 *Control algorithm of the proposed converter during different modes*

speed (ω), and charging power (P_g). Since this work is focused on power electronics converter parts of the electric vehicle; therefore, the mode selection is done manually.

During battery charging from the grid, the reference charging power is divided by instantaneous battery voltage, which is input to the outer proportional-integral (PI) controller $G_{ib}(z)$. The output of the outer PI controller is a reference dc signal for inner controller $G_{iL}(z)$, and multiplied by a unit rectified sinusoidal wave to generate the final reference input to inner current PI controller. The inner current controller is used for the correction of power factor at the grid side.

The output controller $G_{ib}(z)$ is expressed as

$$G_{ib}(z) = K_p + \frac{K_i T_s}{z-1} \tag{25}$$

where K_p is the proportional gain to adjust the control bandwidth and K_i is the integral gain to achieve zero steady-state error.

The inner PI controller is given by the following equation as

$$G_{iL}(z) = K_{pc} + \frac{K_{ic} T_s}{z-1} \tag{26}$$

where K_{pc} is the proportional gain and K_{ic} is the integral gain. These two coefficients should be tuned such that the bandwidth of the controller is kept between one-sixth to one-tenth of the switching frequency. Further, due to presence of low frequency components (100 Hz) in battery current, the bandwidth of $G_{ib}(z)$ controller is kept <100 Hz to avoid the distortion in the reference signal for inner current loop.

In propulsion and regenerative braking mode of operation, average current mode controller is used. Depending upon operating modes appropriate switches are turned ON. In propulsion mode, the dc-link voltage is regulated through two-loop controller. The outer PI controller $G_{hv}(z)$ regulates the dc-link voltage by generating reference battery current for the inner current controller $G_{ibc}(z)$, which is provided by the average current mode controller. In regenerative braking modes, the reference quantity is usually torque. Therefore, torque is converted into reference charging power and this reference power is divided by instantaneous battery voltage, to generate reference battery current, which is input to the current controller $G_{ibc}(z)$ for battery current tracking and as shown in Fig. 7.

7 Results and discussions

7.1 Simulation results

The simulation of the proposed converter has been verified in MATLAB/SIMULINK environment with two sets of circuit parameters, as shown in Table 2.

Set-1: In charging mode, the grid voltage is fixed at 220 V, charging power is 1 kW and the nominal battery voltage is 300 V with 20% of SOC. Fig. 8*a* shows simulated waveforms of grid voltage v_g, grid current i_g, battery voltage V_b, battery current I_b and grid filter voltage and current. In this mode, the proposed converter operates as ZETA PFC converter and it is seen that the grid voltage v_g and grid current i_g are in the same phase with sinusoidal shape while measured total harmonic distortion (THD) of the grid current from fast Fourier transform (FFT) tool of the Matlab is 3.77% and calculated power factor (PF) is 0.99. The battery voltage and current are also shown in Fig. 8*a*. From this figure, it is noticed that the battery current has low-frequency pulsation, which is inherent in single-phase system. This pulsation of battery current I_b depends on filter inductor connected in series with the battery. The inductance value of this filter is compromised between allowable low-frequency battery ripple current and compactness of the charger. The grid side filter capacitor voltage V_{cf} and filter inductor current I_{L_f} are also shown in Fig. 8*a*. The voltage across coupling capacitor C follows battery voltage and both switching and low-frequency voltage ripples are present in *C*.

The relevant waveforms in propulsion mode are shown in Fig. 8*b* with 400 V dc-link and 1 kW output load power. The control objective of this mode is to keep the dc-link constant for satisfactory operation of the inverter drive system. Therefore, dynamic performance of this mode is verified by step load variations from 1 to 2 kW at $t = 1.2$ s and from 2 to 1 kW at $t = 1.8$ s as shown in Fig. 8*c*. Despite the step change in loads at these instants, the dc-link voltage is well regulated at 400 V.

The simulation waveforms of regenerative mode are shown in Fig. 8*d*. To verify this mode, the dc-link voltage is varied manually using bridge rectifier and autotransformer, which is equivalent to the speed change of motor in real-time operation of the vehicle. The variations in the dc-link voltage are between 290 and 350 V and the battery is charged with constant current of 3.5 A. The corresponding variations in duty signal with the dc-link voltage are also shown in Fig. 8*d*. The duty signal is <0.5 whenever, the dc-link voltage is more than the battery voltage, and >0.5 whenever, the dc-link voltage is lower than the battery voltage.

SET-2: In this Set of simulation, the proposed converter is verified at lower voltage and power levels to provide consistency between simulation and hardware results (Section 7.2). The parameters used in this Set are given in Table 2.

In plug-in charging mode, the peak grid voltage is fixed at 100 V, charging power is 230 W and the nominal battery voltage is 60 V with initial battery SOC of 20%. Fig. 9 shows simulated waveforms of this mode. It is seen in Fig. 9*a*, the grid voltage (v_g)

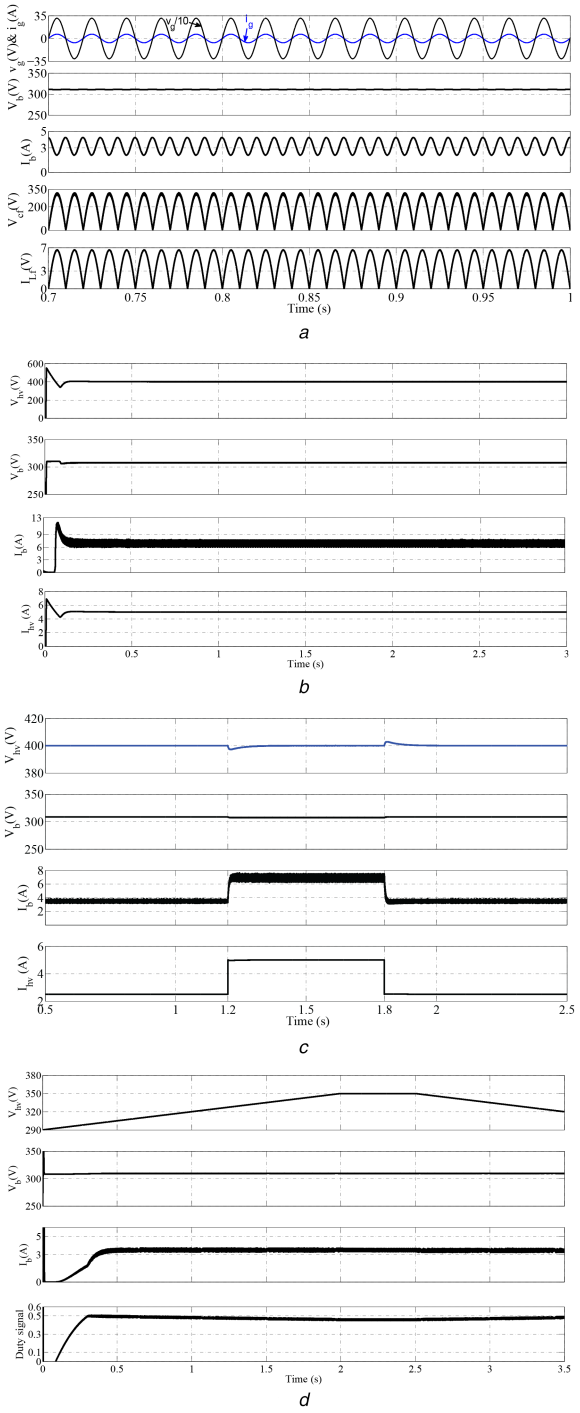

Fig. 8 *Simulation results*

(a) Simulation waveforms during plug-in charging mode with 220 V_{RMS} of grid voltage, ***(b)*** Waveforms of propulsion mode, ***(c)*** Dynamic operation of propulsion mode with step load variations, ***(d)*** Closed loop verification of regenerative braking mode by varying the dc-link voltage

and grid current (i_g) are in the same phase with sinusoidal shape. The measured THD of the grid current and PF are around 3.53% and 0.999, respectively, which demonstrates the effectiveness of the converter operation at lower charging power, grid and battery voltages. The capacitor filter voltage V_{cf} and filter inductor current I_{L_f} are also shown in Fig. 9*a*. In Fig. 9*b*, the voltage across capacitor C, i.e. V_C follows the battery voltage and voltage ripple of this capacitor depends on the battery voltage ripple as well as the value of capacitor C. However, size of capacitor C is compromised between allowable voltage ripple and overall charger size. Moreover, a simulation with 90 V of grid voltage (minimum universal voltage) is also performed, which is shown in Fig. 9*c*.

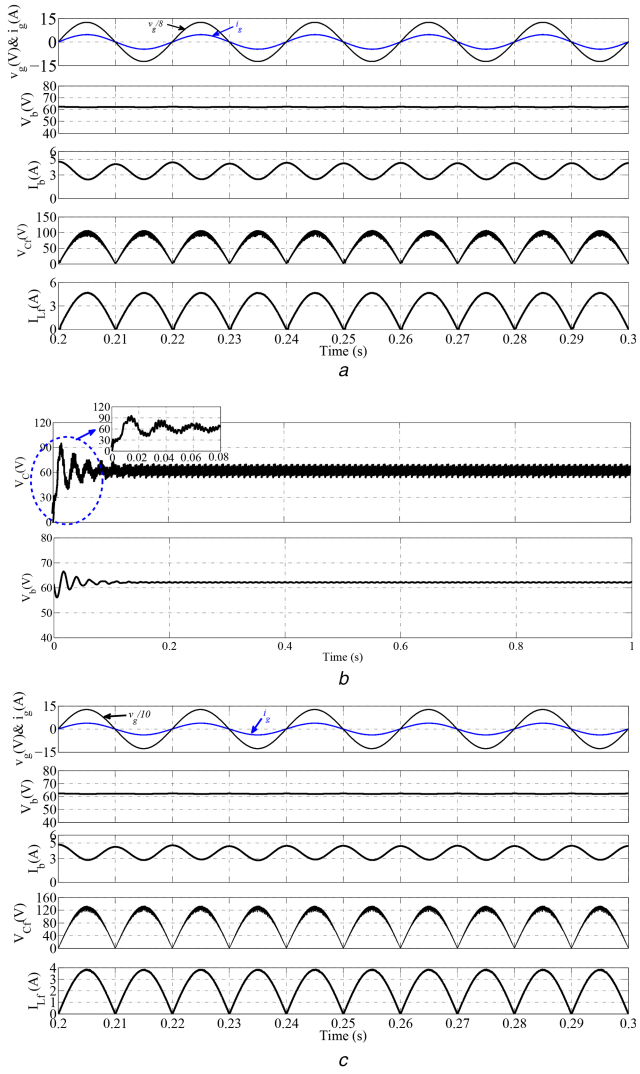

Fig. 9 *Simulation results during plug-in charging mode with 100 V (peak) grid voltage and 60 V battery voltage*

(a) Waveforms of v_g, i_g, V_{C_f} and I_{L_f}, ***(b)*** Waveforms of V_C and V_b, ***(c)*** Simulation results with grid voltage of 90 V

The propulsion mode of operation in this Set is tested with 100 V dc-link voltage (V_{hv}). The simulated waveforms are shown in Fig. 10*a* with 400 W load power. Dynamic operation of the converter in this mode is verified by step change of load at $t = 1$ s, from 200 to 400 W and 400 to 200 W at $t = 2$ s. The dc-link voltage V_{hv} is well regulated (Fig. 10*b*) at reference value even after these load changes, which indicates controllers work effectively at the lower voltage rating.

The regenerative braking mode of this set is verified by linear variations in the dc-link voltage, as shown in Fig. 9*c*. The dc-link voltage is linearly increased from 50 V, $t = 0$ s to 80 V, $t = 2$ s. It is held constant at 80 V between $t = 2$ s and $t = 2.5$ s, after $t = 2.5$ s, it is linearly reduced and the battery is charged with constant current of 3 A. The voltage of capacitor C, V_C follows the battery voltage with ripple contents as shown at bottom of Fig. 10*c*.

7.2 Experimental results

The parameters and specifications of prototype model of the proposed converter are mentioned in Table 6. A field-programmable gate array (FPGA)-based dSPACE (1104) controller is used for the development of the proposed converter. The isolation between controller and gate drivers of semiconductor switches is developed using the optocoupler TLP-250, which can be operated up to 25 kHz. The slow speed of switch body diode is replaced with the fast recovery diode MUR-1560 to reduce the reverse recovery loss and removes unwanted transients of the

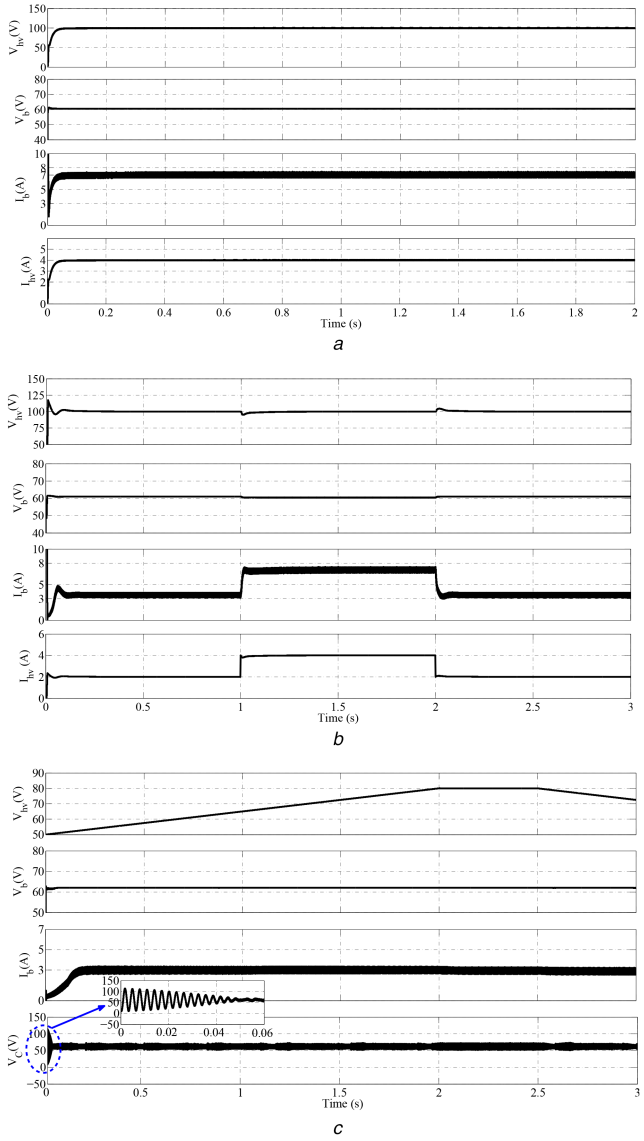

Fig. 10 *Simulation waveforms during propulsion and regenerative braking with 60 V battery and 100 V dc link*

(a) Waveforms in propulsion mode with 400 W load, ***(b)*** Dynamic operation of propulsion mode with load variations, ***(c)*** Closed loop verification of regenerative braking mode by varying the dc-link voltage

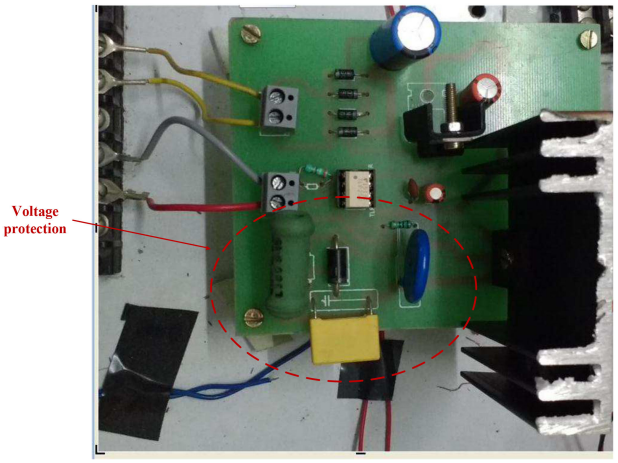

Fig. 11 *Gate driver circuit of switch with voltage protection*

circuit. For voltage protection of the switches, an RC snubber circuit is used along with driver circuit shown in Fig. 11.

During plug-in charging mode, the grid voltage and output battery current are measured using voltage and current sensor, respectively. The dc-link voltage is also measured using voltage sensor. The grid current is measured through an ac current probe of FLUK power analyser. All waveforms are recorded in Agilent Technology, DSO1014A.

Table 6 Experimental circuit parameters

Experimental specifications	
grid voltage (v_g)	42.42/70.7 V
DC-link voltage (V_{hv})	60 V
line frequency (f_L)	50 Hz
battery voltage (V_b)	36 V
battery type	exide power safe plus sealed lead acid
capacity	26 Ah
L_1/L_2	2 mH
$C_{hv}/C_M/C_b$	550/10/2200 μF
power switch	MOSFET IRFP- 460
current sensor	TELCON HTP-25
voltage sensor	AD202JN

Fig. 12 shows waveforms during plug-in charging mode. As we know that in this mode, the battery is charged from the grid supply (60 V peak and 85 W charging power); therefore, converter must operate in PFC mode. In Fig. 12*a*, the grid current at CH1 has nearly sinusoidal shape as well as in phase with the grid voltage at CH2, which shows converter is operating near unity power factor condition. The battery current and voltage are shown at CH3 and CH4, respectively. A low-frequency oscillation in the battery current is seen at CH3 of Fig. 12*a*, if this low-frequency battery current oscillation is high (without output filter), the reverse recovery loss of diode D_6 will increase; therefore, the filter inductor at battery terminal suppresses the oscillation of battery current as well as reduces the reverse recovery loss of the diode D_6, but addition of this filter may depend on manufactures and type of battery (capability to take low-frequency ripple of the battery current). In PFC mode of ZETA converter, it is mandatory to connect an LC filter after rectifier bridge diode to filter out discontinuous input current. The waveforms of filter capacitor voltage and filter inductor current are shown in Fig. 12*b*. Also in Zeta converter voltage across coupling capacitor is same as output voltage, i.e. battery voltage V_b, which is shown in Fig. 12*c*. Fig. 12*d* shows the measured power factor is 0.99, and total harmonic distortion (THD) is 7.1%. The high-power factor operation of the proposed converter relives the burden on grid system and reduces the cost of electricity usages. Furthermore, with 100 V (peak) grid voltage and 85 W charging power (Fig. 13*a*), the measured PF and THD of the grid current are 0.99 and 7.2%, respectively, as shown in Fig. 13*b*. However, the measured input power p_g is 89.5 W at 85 W charging power (P_b); therefore, calculated efficiency is 94.9%. However, with 210 W charging power and 100 V (peak) grid voltage, the measured input power is 226 W (Fig. 13*c*) and calculated efficiency is 92.9%, which is lower compared to 85 W charging power, it is due to fact that conduction losses in MOSFET and inductors significantly increase at higher power. An experimental efficiency curve in charging mode with 60 and 100 V (peak) grid voltages is shown in Fig. 13*d*. The maximum efficiency for 60 V is found to 94.76%. For 100 V, the maximum efficiency is 95.1% at 115 W but it may be more than this value at some other power level.

In propulsion mode, the battery voltage either stepped up or stepped down based on the battery SOC and dc-link voltage range. The objective of this mode is to keep the dc-link voltage constant irrespective of load or supply variations. The screenshot of oscilloscope with 125 W load has been shown in Fig. 14*a*. The dynamic performances of this mode is tested with step change in load variations from 125 to 215 W and corresponding change in battery and load current is shown in Fig. 14*b* at CH3 and CH4, respectively.

In regenerative mode, the battery is charged with regenerative braking energy of motor, the generated voltage is rectified with feedback diodes of the inverter, then depending upon speed of

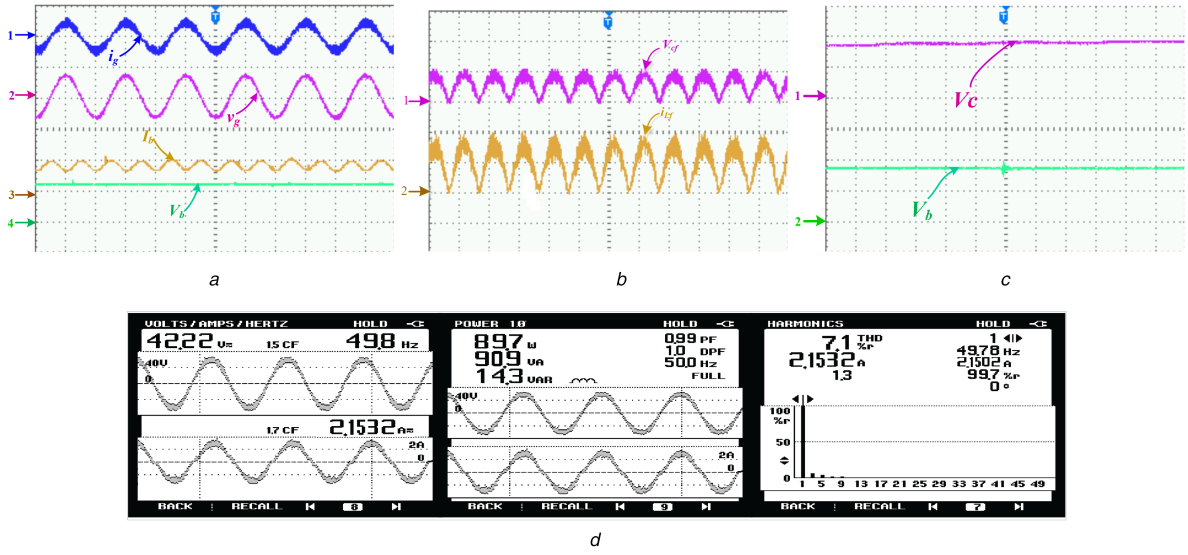

Fig. 12 *Experimental waveforms of plug-in charging mode with 60 V (peak) grid voltage*

(a) Waveforms of grid voltage, grid current, battery current, and battery voltage (CH1: grid current [6 A/div], CH2: grid voltage [100 V/div], CH3: battery current [2.5 A/div], CH4: battery voltage [30 V/div]), time scale = 10 ms/div, ***(b)*** Gris side filter voltage and current (CH1: filter capacitor voltage [30 V/div], CH2: filter inductor current [2 A/div]), time scale = 10 ms/div, ***(c)*** Coupling capacitor and battery voltage (CH1: coupling capacitor voltage [20 V/div], CH2: battery voltage [20 V/div]), time scale = 5 µs/div), ***(d)*** Power quality parameters

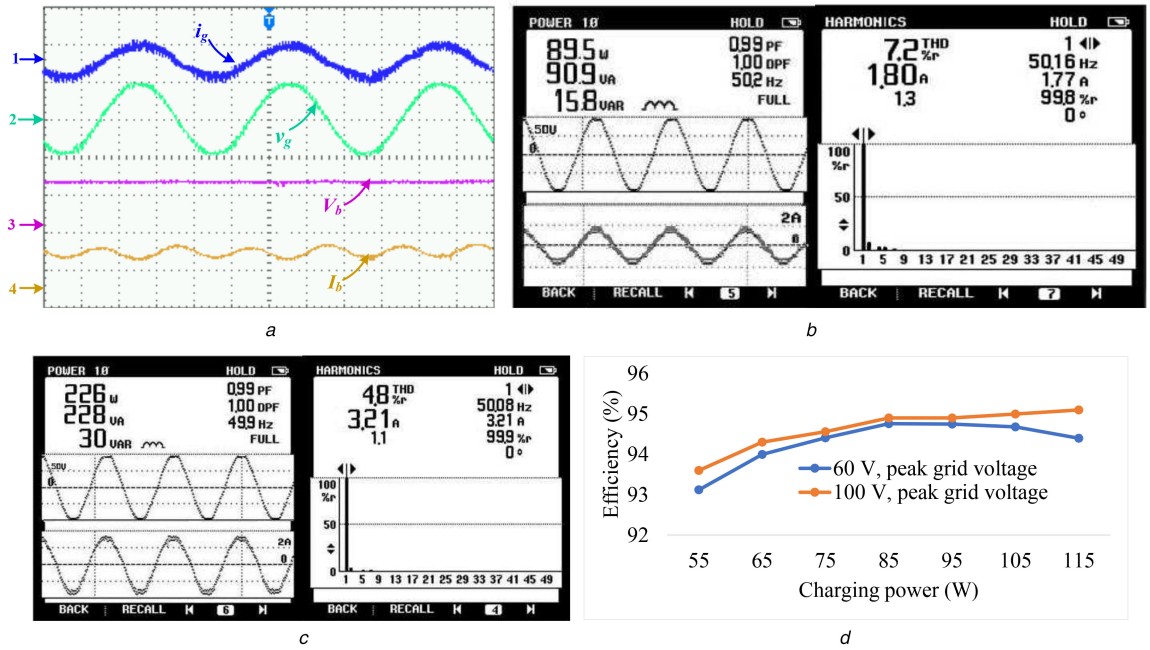

Fig. 13 *Experimental waveforms of plug-in charging mode with 100 V (peak) grid voltage*

(a) Waveforms of grid voltage, grid current, battery current, and battery voltage (CH1: grid current [5 A/div], CH2: grid voltage [100 V/div], CH3: battery current [2.5 A/div], CH4: battery voltage [30 V/div]), time scale = 10 ms/div, ***(b)*** Power quality parameters with 85 W charging power, ***(c)*** With 210 W charging power, ***(d)*** Experimental efficiency of the proposed converter in plug-in charging mode

motor the dc-link voltage varies. However, in this work, this mode is tested by rectifying ac voltage, which is applied through an auto transformer. The relevant waveforms of this mode are shown in Fig. 14*c*. In Fig. 14*c*, the dc-link voltage has been fixed at 70 V, and the battery is charged with 2.78 A of current. In Fig. 14*d*, the dc-link voltage varies from $V_{hv,\min}$ (45 V) to $V_{hv,\max}$ (70 V) and during this variation of the dc-link voltage, the battery current is maintained at 2.78 A through the closed loop operation.

8 Conclusion

In this work, a ZETA-SEPIC-based single-stage power electronics interface has been proposed for PEVs. The proposed converter operates in three modes, i.e. plug-in charging (PFC mode), propulsion and regenerative modes. In PFC and regenerative braking modes, the proposed converter operates as ZETA converter, while in propulsion mode, it operates as SEPIC converter. It means the proposed converter has buck/boost operation in each mode of converter operation without voltage reversal which allows selection of a wide range of the battery voltage, efficient control of dc-link voltage and capturing the regenerative braking energy with wide variations of the motor speed. In comparison with existing single-stage converters, the proposed converter has the least component to those converters which have buck/boost operation in each mode. The functionality and performance of the proposed integrated converter have been verified through both in simulation and hardware. The performance of control algorithm is tested with the step load variations in propulsion mode and dc-link voltage variations in regenerative braking mode. An extensive loss analysis of the proposed converter is investigated to correctly select the power stage switches. The maximum theoretical efficiency of the converter in plug-in

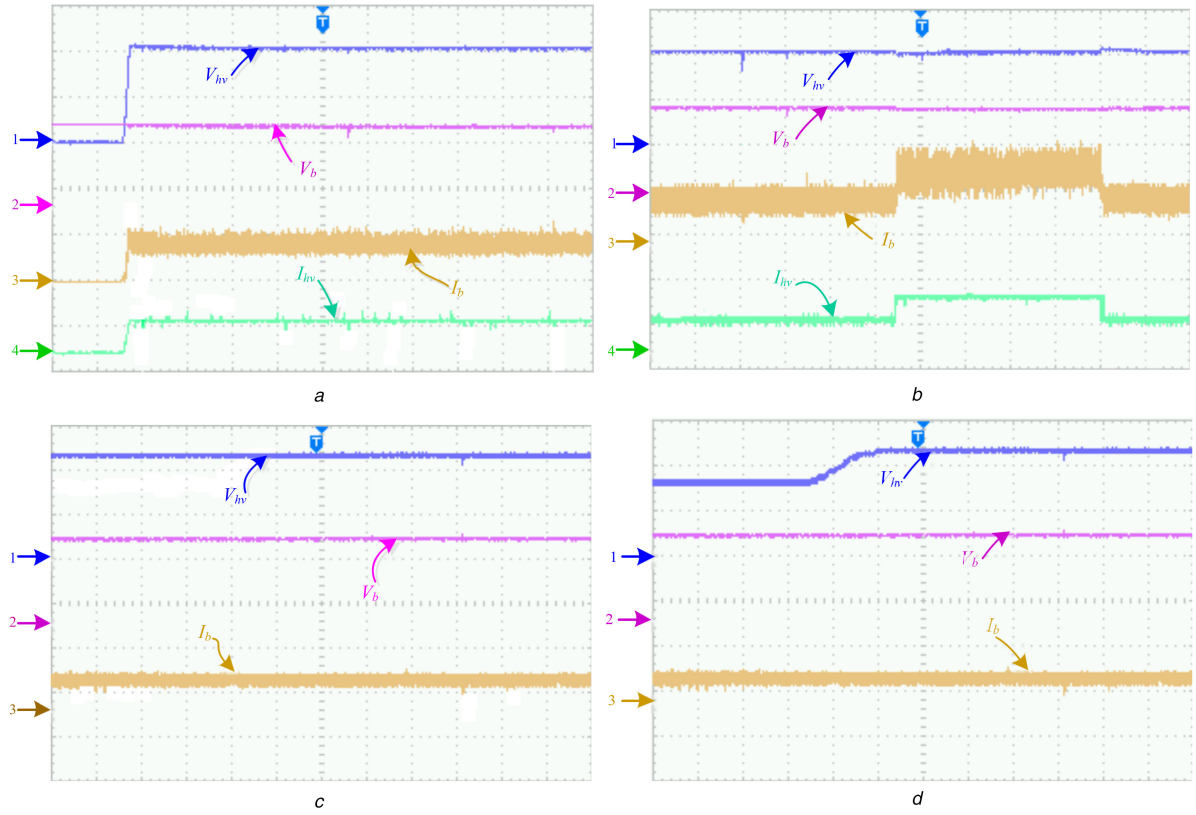

Fig. 14 *Experimental waveforms during propulsion and regenerative modes*

(a) Screenshot of propulsion mode (CH1: dc-link voltage [30 V/div], CH2: battery voltage [20 V/div], CH3: battery current [5 A/div], CH4: dc-link current [3 A/div]), time scale = 1 s/div, ***(b)*** Dynamic performance of propulsion mode (CH1: dc-link voltage [30 V/div], CH2: battery voltage [20 V/div], CH3: battery current[5 A/div], CH4: dc-link current [3 A/div]), time scale = 1 s/div, ***(c)*** Screenshot of regenerative mode (CH1: dc-link voltage [30 V/div], CH2: battery voltage [20 V/div], CH3: battery current [5 A/div]), ***(d)*** Closed loop verification of regenerative mode (CH1: dc-link voltage [30 V/div], CH2: battery voltage [20 V/div], CH3: battery current [5 A/div], time scale = 1 s/div.)

charging, propulsion and regenerative braking modes is found 95.9%, 97.1%, and 96.7%, respectively. While in hardware, the peak efficiency is found 94.76% at 85 W and 60 V peak grid voltage.

9 References

[1] Chan, C.C., Chau, K.T.: 'An overview of power electronics in electric vehicles', *IEEE Trans. Ind. Electron.*, 1997, **44**, (1), pp. 3–13

[2] Emadi, A., Lee, Y.J., Rajashekara, K.: 'Power electronics and motor drives in electric, hybrid electric, and plug-in hybrid electric vehicles', *IEEE Trans. Ind. Electron.*, 2008, **55**, (6), pp. 2237–2245

[3] Singh, A.K., Pathak, M.K.: 'An improved two-stage non-isolated converter for on-board plug-in hybrid EV battery charger'. IEEE 1st Int. Conf. Power Electronics, Intelligent Control and Energy Systems (ICPEICES), 2016. pp. 1–6

[4] Musavi, F., Edington, M., Eberle, W., *et al.*: 'Evaluation and efficiency comparison of front end ac-dc plug-in hybrid charger topologies', *IEEE Trans. Smart Grid*, 2012, **3**, (1), pp. 413–421

[5] McGrath, B.P., Holmes, D.G., McGoldrick, P.J., *et al.*: 'Design of a soft-switched 6-kW battery charger for traction applications', *IEEE Trans. Power Electron.*, 2007, **22**, (4), pp. 1136–1144

[6] Aharon, I., Kuperman, A.: 'Topological overview of powertrains for battery-powered vehicles with range extenders', *IEEE Trans. Power Electron.*, 2011, **26**, (3), pp. 868–876

[7] Qian, W., Cha, H., Peng, F.Z., *et al.*: '55-kW variable 3X DC-DC converter for plug-in hybrid electric vehicles', *IEEE Trans. Power Electron.*, 2012, **27**, (4), pp. 1668–1678

[8] Park, T., Kim, T.: 'Novel energy conversion system based on a multimode single-leg power converter', *IEEE Trans. Power Electron.*, 2013, **28**, (1), pp. 213–220

[9] Lee, Y.J., Khaligh, A., Emadi, A.: 'Advanced integrated bidirectional AC/DC and DC/DC converter for plug-in hybrid electric vehicles', *IEEE Trans. Veh. Technol.*, 2009, **58**, (8), pp. 3970–3980

[10] Dusmez, S., Khaligh, A.: 'A compact and integrated multifunctional power electronic interface for plug-in electric vehicles', *IEEE Trans. Power Electron.*, 2013, **28**, (12), pp. 5690–5701

[11] Dusmez, S., Khaligh, A.: 'A charge-nonlinear-carrier-controlled reduced-part single-stage integrated power electronics interface for automotive applications', *IEEE Trans. Veh. Technol.*, 2014, **63**, (3), pp. 1091–1103

[12] Tang, Y., Zhu, D., Jin, C., *et al.*: 'A three-level quasi-two-stage single-phase PFC converter with flexible output voltage and improved conversion efficiency', *IEEE Trans. Power Electron.*, 2015, **30**, (2), pp. 717–726

[13] Kong, P.Y., Aziz, J.A., Sahid, M.R., *et al.*: 'A bridgeless PFC converter for on-board battery charger'. IEEE Conf. Energy Conversion (CENCON), 2014, pp. 383–388

[14] Shi, C., Wang, H., Dusmez, S., *et al.*: 'A SiC-based high-efficiency isolated onboard PEV charger with ultrawide dc-link voltage range', *IEEE Trans. Ind. Appl.*, 2017, **53**, (1), pp. 501–511

[15] Patil, D., Sinha, M., Agarwal, V.: 'A CuK converter based bridgeless topology for high power factor fast battery charger for electric vehicle application'. IEEE Transportation Electrification Conf. Expo (ITEC), 2012, pp. 1–6

[16] Patil, D., Agarwal, V.: 'Compact onboard single-phase EV battery charger with novel low-frequency ripple compensator and optimum filter design', *IEEE Trans. Veh. Technol.*, 2016, **65**, (4), pp. 1948–1956

[17] Oh, C.Y., Kim, D.H., Woo, D.G., *et al.*: 'A high-efficient nonisolated single-stage on-board battery charger for electric vehicles', *IEEE Trans. Power Electron.*, 2013, **28**, (12), pp. 5746–5757

[18] Musavi, F., Eberle, W., Dunford, W.G.: 'A high-performance single-phase bridgeless interleaved PFC converter for plug-in hybrid electric vehicle battery chargers', *IEEE Trans. Ind. Appl.*, 2011, **47**, (4), pp. 1833–1843

[19] Egan, M.G., O'Sullivan, D.L., Hayes, J.G., *et al.*: 'Power-factor-corrected single-stage inductive charger for electric vehicle batteries', *IEEE Trans. Ind. Electron.*, 2007, **54**, (2), pp. 1217–1226

[20] Bai, H., Zhang, Y., Semanson, C., *et al.*: 'Modelling, design and optimisation of a battery charger for plug-in hybrid electric vehicles', *IET Electr. Syst. Transp.*, 2011, **1**, (1), pp. 3–10

[21] Morcos, M.M., Dillman, N.G., Mersman, C.R.: 'Battery chargers for electric vehicles', *IEEE Power Eng. Rev.*, 2000, **20**, (11), pp. 8–11, 18

[22] Kim, J.S., Choe, G.Y., Jung, H.M., *et al.*: 'Design and implementation of a high-efficiency on- board battery charger for electric vehicles with frequency control strategy'. IEEE Vehicle Power and Propulsion Conf., 2010, pp. 1–6

[23] Singh, S., Singh, B., Bhuvaneswari, G., *et al.*: 'Power factor corrected zeta converter based improved power quality switched mode power supply', *IEEE Trans. Ind. Electron.*, 2015, **62**, (9), pp. 5422–5433

[24] Vlatkovic, V., Borojevic, D., Lee, F.C.: 'Input filter design for power factor correction circuits', *IEEE Trans. Power Electron.*, 1996, **11**, (1), pp. 199–205

[25] Mahdavi, M., Farzanehfard, H.: 'Bridgeless SEPIC PFC rectifier with reduced components and conduction losses', *IEEE Trans. Ind. Electron.*, 2011, **58**, (9), pp. 4153–4160

[26] Singh, S., Singh, B., Bhuvaneswari, G., *et al.*: 'A power quality improved bridgeless converter-based computer power supply', *IEEE Trans. Ind. Appl.*, 2016, **52**, (5), pp. 4385–4394